A stochastic model for the aerodynamics of irregularly shaped gravel

M. S. Ahsanullah

Glenn Department of Civil Engineering, Lowry Hall, Clemson University, Clemson, SC, USA, 29634

N. B. Kaye

Glenn Department of Civil Engineering, Lowry Hall, Clemson University, Clemson, SC, USA, 29634

W. C. Bridges

Department of Mathematical and Statistical Sciences, Martin Hall, Clemson University, Clemson, SC, 29634

Abstract

The flight of compact debris can be highly stochastic in nature. However, standard flight equations are deterministic after assuming a spherical shape for gravel. This study proposes a stochastic model to resolve some key aspects of these uncertainties that originate due to changes in orientation of the debris particle during flight. The model numerically solves the differential equations of motion for a large number of gravel pieces taken from five different size gradations. The amount by which the drag and lift coefficients (δC_D and δC_L), the lift force direction ($\delta\theta$) and the projected area ($\delta\alpha$) are varied at each time-step during the flight simulation of a single debris are the four parameters used to fit the model to the results obtained from gravel drop experiments. An optimization criterion (ϵ) was introduced and the model was optimized for each gravel gradation tested. It was found that only small perturbations in the lift coefficient are needed to model the flight. However, larger perturbations in the direction of the lift force are required to correctly predict the statistics of the landing locations.

Keywords: Windborne debris; Compact debris; stochastic modeling; Gravel;

1. Introduction

1.1. Role of wind-borne debris

Wind-borne debris and missiles in hurricanes and other strong wind events have been observed to cause significant damage to the built environment. After more than thirty years of research on hundreds of post-storm investigations, Minor (2005) [1] has concluded that the building envelope is crucial to satisfactory performance of buildings in windstorms and wind-driven debris is a decisive factor in determining the performance of the building envelope. Field investigations show how the entire structure of a building can suffer from cascading failure following the first failure of the envelope. Leakage of the building envelope due to impact by fast-moving debris exposes the conditioned space within the building to the external unconditioned environment. This results in increased rain and debris infiltration, causing further damage to the contents within the interior of the building. This can also lead to internal pressurization and increased roof uplift, which can, in severe cases, cause roof lift-off. Smith & McDonald (1990) [2] stated in their report following Hurricane Hugo (Charleston, SC-1989) that, the damage to the inside of the building and the contents within due to water infiltration can cause greater financial loss than the damage to the building structure itself. Thorough assessments of insurance records following strong wind events also show a dramatic increase in the total financial loss for damage that involves breaching of the building envelope. Sparks et al. (1994) [3] related wind speed to the damage claims and concluded that the size of claims is greater when the building envelope is compromised in the event of storms and hurricanes.

There have been extensive studies and literature for decades, corroborated by thorough post-hurricane investigations, on the role of wind-borne debris on the built environment. Reports after notable wind events such as Hurricane Hugo (1989, Charleston SC), Hurricane Andrew (1992, South Florida), and Hurricane Alicia (1983, Houston TX) show that wind-borne debris had been a

major contributor to the total economic loss [1]. Several studies following Hurricane Alicia have shown that blown-off roof gravel caused significant damage to the windows of high-rise buildings in Downtown Houston. Behr & Minor (1994) [4] have also drawn similar conclusions after Hurricane Andrew, which caused an estimated total of US$ 26.5 billion in damage according to the report by the United States National Hurricane Center [5]. In their report one year after Hurricane Hugo, Smith & McDonald (1990) [2] have shown that the blown-off gravel can cause severe injury and property damage, and in one case, aggregate has been recorded to have traveled more than 245 ft (75 m) from one building to another breaking nearly all of the outer panes of double-glazed windows and a number of inner panes as well. Roof gravel blow-off during Hurricane Katrina resulted in the destruction of the front facade of the Hyatt Hotel in downtown New Orleans, LA,[6] resulting in significant damage, loss of revenue during repair, and an initial insurance claim of $100m[7]. Broken windows due to windborne debris can lead to internal pressurization of the structure potentially resulting in significant structural damage such as roof lift off [3]. Such breaches in the building envelope can also result in rainfall penetration of the structure causing water damage to the contents [8].

In an attempt to address the issue of damage from wind-borne debris, building design codes have gone through several modifications over time and the existing design guidelines have still proven to fall short at times with debris motion initiation occurring at wind speeds lower than the design wind speeds. There still exists a significant knowledge gap around the motion initiation mechanism and resulting flight. These criteria can be solved only with a deeper understanding of the forces acting on individual particles of randomly shaped compact debris.

1.2. Debris classification

Debris has been classified in different ways based on their shape, size, weight and locations. However, the most commonly used scheme of debris classification while modeling debris flight, proposed by Wills et al. (2002) [8], classifies

the debris in three types (shown in Figure 1) based on their geometric shape: rod-like (linear debris), plate-like (planar debris) and compact debris (three dimensional debris). Rod-like debris has one dimension significantly larger than the other two, Plate-like debris has two dimensions significantly larger than the third one, and Compact debris has similar dimensions in all three directions.

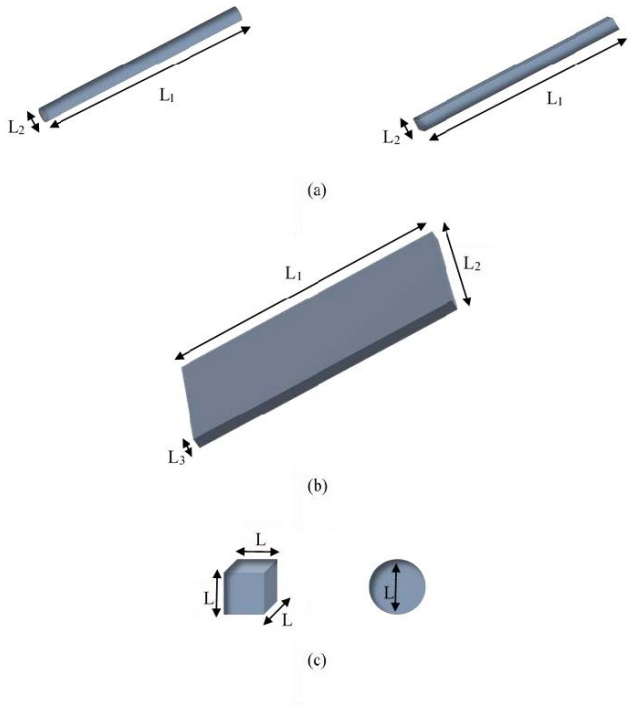

Figure 1: Classification of Debris with dimensions (a) Rod-like Debris ($L_1 >> L_2$), (b) Plate-like Debris ($L_1, L_2 >> L_3$), (c) Compact Debris ($L_1 \approx L_2 \approx L_3 \approx L$)

.

The standard compact debris flight equations assume that the debris can be treated as spherical [9, 10] and that it does not rotate. The consequences of these assumptions are that

1. There are no aerodynamic moments acting on the debris
2. There are no lift forces acting on the debris,
3. The debris cross-sectional area is independent of orientation, and, therefore,

4. The only forces acting on the debris are the debris weight (vertically down) and aerodynamic drag acting in the direction of the apparent wind.

These assumptions lead to the derivation of the compact debris flight equations which, for a straight-line wind, are two dimensional. They can be written as a set of two coupled second order ordinary differential equations

$$\frac{d^2x}{dt^2} = \frac{du}{dt} = \frac{\rho C_D A}{2m}(U-u)\sqrt{(U-u)^2+w^2} \tag{1}$$

and

$$\frac{d^2z}{dt^2} = \frac{dw}{dt} = \frac{\rho C_D A}{2m}(-w)\sqrt{(U-u)^2+w^2} - g \tag{2}$$

In the above equations x is the horizontal coordinate in the direction of the wind flow, z is vertically upward, m is the mass of the debris, ρ is the fluid density, C_D is the drag coefficient (often assumed to be constant), g is acceleration due to gravity, U is the wind speed (commonly taken to be uniform and horizontal), and u and w are the horizontal and vertical components of the debris particle velocity respectively. For a long enough flight distance these equations yield a solution in which the debris travels horizontally at the wind speed and vertically at its terminal velocity. However, irregularly shaped compact debris does not travel in a two-dimensional plane. This can be observed by dropping small pieces of gravel into a tank of water and observing that they do not fall vertically. Observations from such experiments indicate that

1. the gravel pieces change orientation during their fall
2. their fall is not vertical or, in fact, even in a straight line, and
3. the path varies from one piece to the next even for gravel pieces taken from the same gravel gradation.

When a piece of gravel is released from rest it will initially fall vertically because the only forces acting on it are its weight down and the buoyancy force up (assumed negligible when falling through air, but significant when falling

through water). At this point the apparent fluid velocity, that is, the fluid velocity relative to the gravel, will be vertically up. Therefore, any deviation of the flight path from vertical must be the result of a lift force (i.e. an aerodynamic force that acts normal to the direction of the apparent fluid velocity). Further, since the gravel is observed to change orientation during flight, the cross-sectional area of the gravel normal to the apparent fluid velocity will vary. These observations violate all four of the assumptions listed above for using the compact debris flight equations.

To better understand the flight of irregularly shaped compact debris, an experimental and modeling study was undertaken and is presented below. In section 2 the experimental methods are described including details of the data collection and analyses. Experimental results are presented in section 3 including qualitative descriptions of the flight paths and statistical analysis of the landing locations of the various gravel pieces dropped. These observations are used to develop a stochastic flight model for gravel pieces falling through a stagnant environment (section 4). The results are discussed in section 5, and conclusions are drawn in section 6.

2. Experimental methods

2.1. Experimental setup

To gain insight on the motion of irregularly shaped gravel pieces moving through a fluid, a simple experimental setup is designed for this study. The setup consists of a clear-sided tank filled with water and gravel pieces of different sizes as representative of a typical compact debris (shown in Figure 2).

The main objective of the experiment is to observe the distribution of the landing locations of dropped gravel pieces. An earth-fixed, right-handed coordinate system is defined with its origin fixed at the center of the cross-section of the tank. The x and y-axes are on the horizontal plane as shown in Figure 3 while the z-axis points vertically upwards with its origin at the water surface where the particles are released.

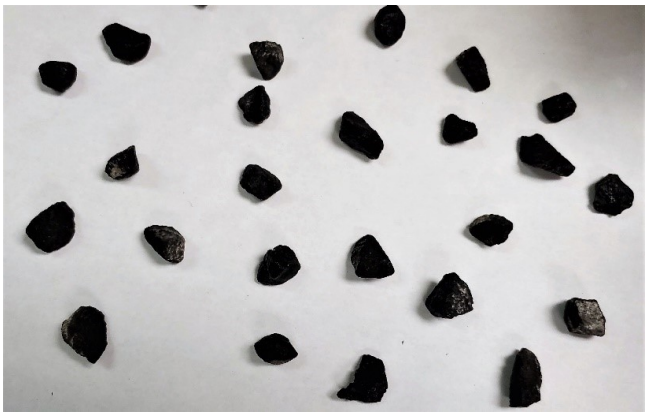

Figure 2: Some samples of the gravel pieces used in the experiment taken from gradation E.

.

2.2. Experimental Procedure

To locate the center of the cross-section (the origin), fishing wire was stretched from corner to corner diagonally. Each piece of gravel was released from the center, directly below the point where the wires intersect each other. The gravel was held by a pair of tweezers and released slightly below the water surface such that the gravel was just submerged and stationary when released. The orientation of the gravel at the release point was varied to avoid any systematic bias in the initial conditions.

A thin uniform layer of sand was placed on the bottom of the tank to prevent gravel pieces from bouncing off the floor when they land. For each gravel size, sets of 20 pieces were dropped consecutively. After each set of 20 drops, an aerial photo of the spread was taken from directly above the fish tank for further analyses. A total of 200 drops were done for each gravel gradation. Each particular set of drops was limited to 20 pieces before photographing and removing the gravel from the sand bed. This was done to avoid having particles land on top of or bounce off a previously dropped piece.

From each plan view photo, the landing locations were digitized as a scatter plot with respect to a given 2D coordinate system. From the resulting x-y coordinates of the landing locations, the radial distance from the center of the

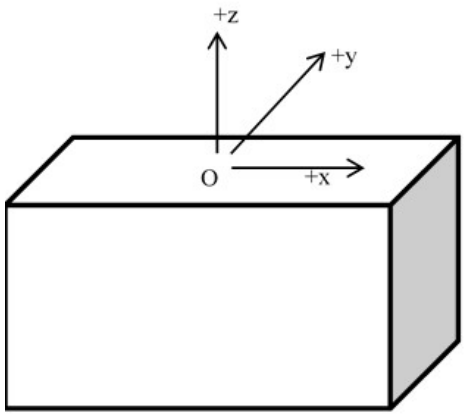

Figure 3: Schematic diagram of the water tank and the system of coordinates. The tank had an internal length of 59 cm, a width of 29.2 cm and a height of 40 cm. The distance from the water surface to the top of the sand layer was 37.5 cm.

tank base (directly below the release point at $x = y = 0$) to each landing location was calculated. The landing locations were calculated using ScanIt [11]. This software takes an image file and allows the user to create a 2D coordinate system. Based on this defined coordinate system, each landing location is assigned a pair of x-y coordinates which can be exported to a spreadsheet. The radial distances of the landing locations from the center of the tank base is calculated using the exported data. Figure 4 below shows the user interface of the software.

2.3. Statistical Description of Gravel Size and Shape

For the experiments in this study, five different sizes of gravel have been used denoted as gradations A, B, C, D and E from largest to smallest size in order of their mean equivalent radii. For each of the five gravel sizes, a sample of 45 pieces was randomly selected, and lengths along the shortest dimension (L_1), the longest dimension (L_3) and in the direction perpendicular to L_1 and L_3 were measured (L_2). Figure 5 shows a representation of L_1, L_2 and L_3 measurements for a sample gravel piece.

Both L_1 and L_2 were, then, normalized by the longest dimension (L_3) to assess the size variation across the gravel gradations. The mean volume of the

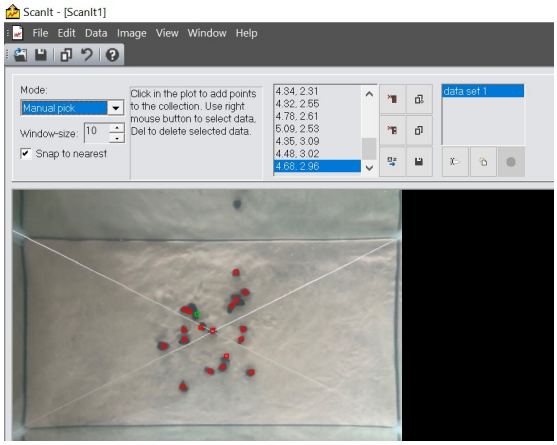

Figure 4: User interface of ScanIt showing extraction of coordinates for landing locations from a sample aerial photo.

gravel pieces for each gradation was calculated by placing a number of gravel pieces in water inside a measuring cylinder and observing the volume of displaced water. From the mean volumes, mean equivalent radii for all the gradations are calculated from the expression of the volume of a sphere. Table 1 shows a summary of all these measurements.

To understand how the two aspect ratios vary for each gradation compared to another, and to understand whether or not there is some form of geometric similarity across the gradations, L_2/L_3 for each gradation is plotted against L_1/L_3 and the resulting spread was observed qualitatively. Figure 6 shows the plots obtained for each gradation:

In figure 6 it can be clearly observed that the spreads vary noticeably across the gradations. The spread for gradation C seems to be quite localized compared to the others. The ratio L_1/L_3 for gradation C seems to lie mostly between 0.25 and 0.7, while L_2/L_3 varies between 0.45 and 0.95. The same ratios for other gravels are more spread apart (e.g. $0.2 \leq L_1/L_3 \leq 0.85$ and $0.3 \leq L_2/L_3 \leq 1.0$ for gradation B). The spreads for A and B can be seen to be more skewed towards the upper right region of the plot. Histograms obtained from the two ratios for all gradations also illustrate similar differences (Figure 7).

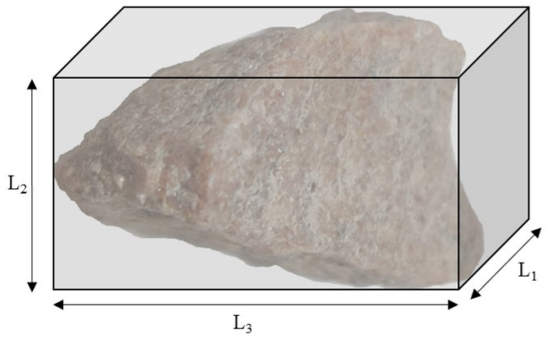

Figure 5: A gravel piece with bounding cuboid showing length measurements along the three directions (L_1, L_2 and L_3).

The distribution of L_1/L_3 is clearly peaked in the middle with little spread on either side for gradation C, and L_2/L_3 has a peak that has a higher frequency than the other gradations and skews towards the right. For both ratios, there are relatively fewer occurrences further away from the peak compared to other gradations. From this analysis, we can make a qualitative observation that the aspect ratios and, therefore, the overall shapes and central tendencies of the distributions appeared to differ across the gradations studied. This observation is further checked by performing a single-factor MANOVA (Multivariate Analysis of Variance) from which we obtained a p-value below the significance level, $\alpha_{sig} = 0.05$, which quantitatively proves that the differences of means across the gradations are statistically significant (details of the MANOVA are in Appendix A). Therefore, given the lack of geometric similarity, one would not expect the resulting distribution of landing locations to be similar across the gradations tested.

3. Experimental results

During the experiment, the trajectory of the dropped gravel was carefully observed. These observations leads to several findings: (1) gravel continuously changes its orientation during its fall, (2) their path of travel is neither linear, nor vertical, and (3) for gravel pieces taken from the same gradation, each piece has

Gravel Size	**A**	**B**	**C**	**D**	**E**
R_e **(mm)**	7.10	5.68	5.60	3.58	1.99
mean L_1 **(mm)**	9.99	8.82	8.02	4.21	2.86
mean L_2 **(mm)**	16.64	12.75	12.28	7.56	4.62
mean L_3 **(mm)**	21.13	18.02	17.69	10.55	7.18
mean $\frac{L_1}{L_3}$	0.49	0.51	0.46	0.42	0.42
St. Dev. $\frac{L_1}{L_3}$	0.13	0.16	0.11	0.14	0.13
mean $\frac{L_2}{L_3}$	0.80	0.73	0.71	0.73	0.67
St. Dev. $\frac{L_2}{L_3}$	0.12	0.16	0.12	0.15	0.14

Table 1: Summary of all the dimension measurements for gravel gradations A through E

a different trajectory. All these findings contradict the underlying assumptions in the standard compact debris flight equations. The standard debris flight equations for compact debris treat compact debris as spherical objects that are not rotating [9, 10]. This assumption fails to take the aerodynamic moments and lift forces into account which results in a 2D motion in straight-line winds. The experimental findings, however, show otherwise as seen in a series of frame-by-frame pictures of a single gravel drop in Figure 8.

Initially, as a gravel piece is released from rest, it will fall vertically downwards as long as the only two forces acting on it are weight (vertically down) and buoyancy (vertically up). Since the velocity of the fluid relative to the gravel is vertically upwards at this point, any subsequent deviation of the piece from vertical is associated with the presence of a lift force acting on it in a direction perpendicular to its velocity at any given point. Moreover, the change in orientation of gravel pieces during their fall shows that the projected cross-sectional area of the gravel normal to the apparent fluid velocity will continue to vary during the fall. Due to these factors, the resulting landing locations for a number of dropped gravel pieces will be spread around the center of the tank

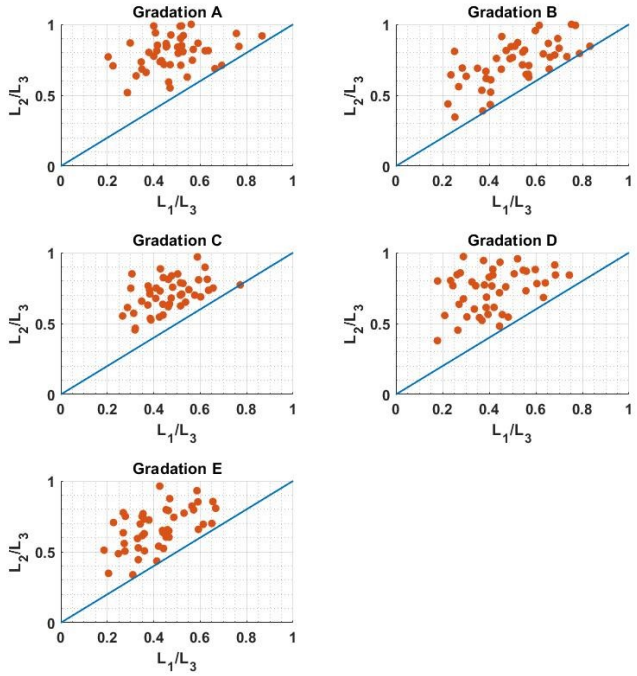

Figure 6: L_2/L_3 vs L_1/L_3 scatter plots showing the distribution of the two aspect ratios for each gradation. The blue lines have a slope of 1 and mark the lower bounds on the data.

base as shown in Figure 4.

The mean and standard deviation of the radial distances of these landing locations measured from directly below the release point. These statistics are recorded in Table 2. Figure 9 shows a histogram of the radial distances for 200 drops for one gravel gradation (gradation A).

From the histogram in Figure 9, we observe that the peak has a finite non-zero value. This implies that only a few pieces actually land close to directly below the release point, rather, in most cases, the path traveled by the dropped gravel pieces are not vertical. This is qualitatively similar to the drop experiments of Tohidi & Kaye (2017) [12] for rod-like debris.

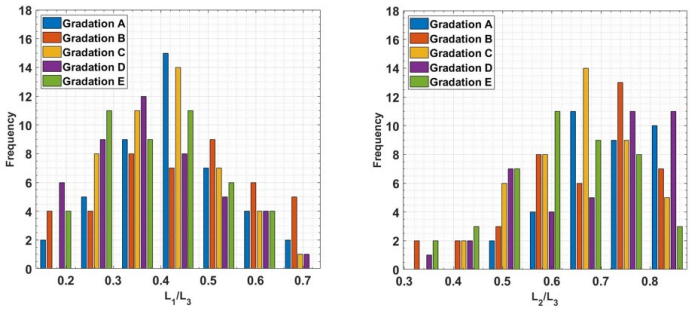

Figure 7: Histograms showing the spread of the two aspect ratios (L_1/L_3 and L_2/L_3).

Gradation	A	B	C	D	E
Mean [mm]	56.7	38.9	52.8	48.6	30.1
St. Dev. [mm]	30.0	28.5	32.2	30.8	22. 3

Table 2: Means and standard deviations of radial distances obtained from experiments for all the gradations

4. Model development

This section describes the development and optimization of a stochastic compact debris flight model that accounts for variation in gravel geometry, variation in orientation during flight, and lift forces generated from asymmetry in the gravel shape and rotation during flight.

4.1. Model equations

In order to develop a 3-D debris trajectory model, it is necessary to define a fixed system of coordinates to track the motion of gravels in 3-D space. Figure 3 shows the fixed, right-handed coordinate system that has its origin placed at the release point for the experiments and the same coordinate system is used in the model development. The position and velocity vectors for the center of a given gravel piece are given by the position $\mathbf{x} = [x, y, z]$ and velocity, $\mathbf{u} = [u_x, u_y, u_z]$ respectively. While the gravel pieces are observed to change orientation during their falls the model assumes that the rotation only contributes to changes in

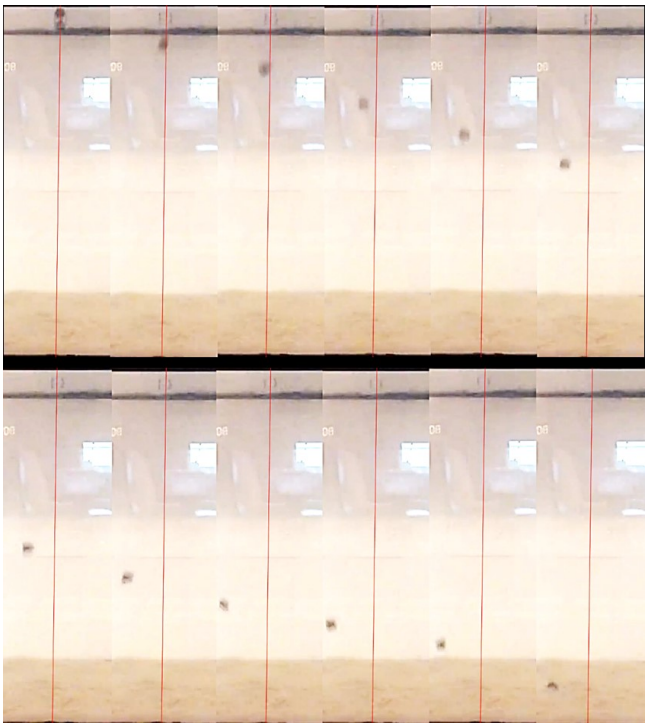

Figure 8: Series of 12 frame-by-frame images, showing a single piece of gravel falling through water. The vertical red lines correspond to the release location.

the magnitude of the drag force (through changes in cross-sectional area and C_D) and the magnitude and direction of the lift force. As the drag and lift forces are modelled stochastically there is no need to explicitly model the aerodynamic moments and resulting rotation.

This modeling approach is conceptually similar to that of Grayson et al. (2012) [13], who developed a six degree-of-freedom stochastic model for plate-like debris flight. In their model the debris location and orientation was randomly perturbed each time step while integrating deterministic 6 DOF flight model. In the model presented below we randomly perturb the equation parameters each time step and then calculate the location which is treated as deterministic for a given set of equation parameters.

The equations that govern the motion of these particles are the rectilinear

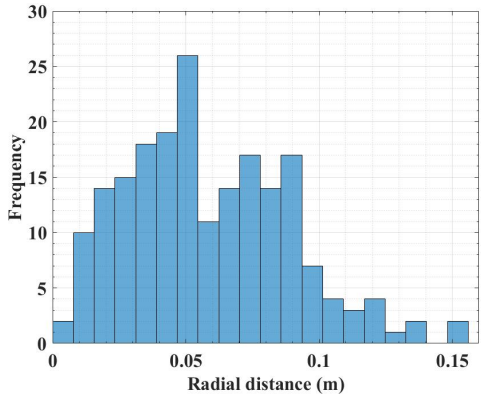

Figure 9: Histogram of radial distances of landing locations for gradation A.

equations of motion in three dimensions:

$$\frac{d^2\mathbf{x}}{dt^2} = \frac{d\mathbf{u}}{dt} = \frac{\mathbf{F_w} + \mathbf{F_B} + \mathbf{F_L} + \mathbf{F_d}}{m} \tag{3}$$

where bold symbols represent Cartesian vectors, and the velocity vector ($\mathbf{u}$) is given by

$$\mathbf{u} = \frac{d\mathbf{x}}{dt} \tag{4}$$

and m is the mass of the gravel piece. The forces acting on the gravel are the drag force,

$$\mathbf{F_d} = -\frac{1}{2}\rho A|\mathbf{u}|\mathbf{u}C_D, \tag{5}$$

lift force,

$$\mathbf{F_L} = \frac{1}{2}\rho A|\mathbf{u}|^2 C_L \mathbf{n_L}, \tag{6}$$

weight,

$$\mathbf{F_w} = (0, 0, -mg), \tag{7}$$

and buoyancy force,

$$\mathbf{F_B} = (0, 0, \rho\forall g). \tag{8}$$

Herein ρ is the density of the fluid, A is a characteristic cross-sectional area of the gravel, C_D and C_L are drag and lift coefficients respectively, g is acceleration due to gravity, $\forall$ is a characteristic volume of the gravel and $\mathbf{n_L}$ is a unit vector

in the direction of lift force. See Figure 10 for the kinematic and free body diagrams. Solving the coupled equations (3) and (4) leads to the velocity and position of the gravel piece as a function of time.

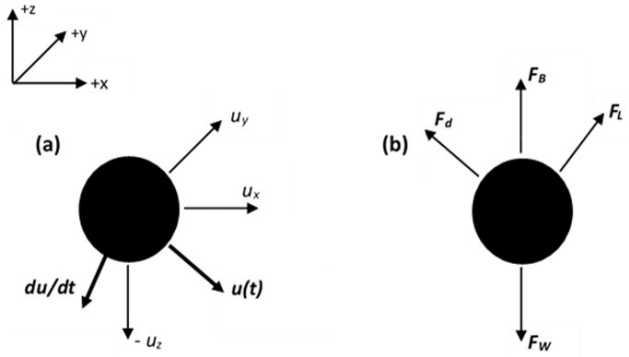

Figure 10: (a) Velocity diagram showing the velocity components in x, y and z directions. (b) Free body diagram.

4.2. Model parameters

For any given collection of gravel pieces, even if from the same gradation, the values of A and $\forall$ will vary from piece to piece. During flight, changes in orientation mean that the area normal to the apparent fluid velocity will vary over time. Changes in orientation will also lead to variation in the force coefficients C_D and C_L and the direction of the lift force $\mathbf{n_L}$. Finally, the initial values of all these parameters will vary depending on the orientation of the gravel upon release from rest. It is highly likely that, even if all these parameters were known explicitly as a function of orientation, it would still not be possible to predict the trajectory as the results would be so sensitive to the initial release angle that, in the absence of perfect knowledge of the release, it would not be possible to predict an individual flight path [12]. Therefore, the model development is focused on predicting the statistical properties of a large number of trajectories for gravel pieces released under nominally identical conditions. To do this, A, C_D, C_L and $\mathbf{n_L}$ are treated as randomly varying parameters in the model.

The ranges, within which C_D and C_L are varied in this study, are determined based on the work of Chai et al. (2018) [14] whose measurements showed values of C_D and C_L vary over the ranges $0.4 < C_D < 0.8$ and $0 < C_L < 0.35$ respectively for a range of different rock pieces oriented in different directions. Given that the force coefficients are functions of an unknown orientation and we have no knowledge of the distribution of orientation during flight, we assume that they are both uniformly distributed between the limits given.

The area A was taken to have a reference value given by

$$A_R = \pi R_e^2 \tag{9}$$

where, R_e is the equivalent radius of the average gravel piece in a given gradation. It is defined as the radius of the sphere that has the same volume as the average gravel piece. The range of possible areas is taken to be

$$\bar{L_1}\bar{L_2} \leq A \leq \bar{L_2}\bar{L_3} \tag{10}$$

where $\bar{L_1}$, $\bar{L_2}$, and $\bar{L_3}$ are the averages of the shortest, intermediate, and longest gravel dimensions respectively as defined in section 2. This area calculation assumes that the gravel is cuboid (see figure 5) and will, therefore, overestimate the areas. However, this overestimation is offset by using the average length values such that there will be gravel pieces for which $\bar{L_1}\bar{L_2}$ and $\bar{L_2}\bar{L_3}$ are outside the bounds assumed for A. The area value used in the model is

$$A = \alpha A_R \tag{11}$$

where, α is a random variable uniformly distributed over the range

$$\frac{\bar{L_1}\bar{L_2}}{A_R} \leq \alpha \leq \frac{\bar{L_2}\bar{L_3}}{A_R} \tag{12}$$

As the model does not calculate orientation, the direction of the lift force is only known to be normal to the apparent fluid velocity. However, this criterion only identifies the plane normal to the velocity vector. A specific unit vector, $\mathbf{n_L}$, is generated by first defining a reference unit vector ($\mathbf{n_{ref}}$) in the global $x - y$ plane

$$\mathbf{n_{ref}} = (sin\theta, cos\theta, 0) \tag{13}$$

in which θ is randomly generated at the start of each flight from a uniform distribution over the range $0 \leq \theta < 2\pi$. The unit vector normal to the direction of the apparent fluid motion is calculated by taking the cross product of the unit vector in the direction of the velocity with the reference unit vector

$$\mathbf{n_L} = \frac{\mathbf{u(t)}}{|\mathbf{u(t)}|} \times \mathbf{n_{ref}} \tag{14}$$

Therefore, the lift force vector in three dimensions takes the following form

$$\mathbf{F_L} = \frac{1}{2}\rho A|\mathbf{u}|\mathbf{u}C_L \times \mathbf{n_{ref}} \tag{15}$$

The coupled governing differential equations (3) and (4) are numerically solved in MATLAB using a 4th order Runge-Kutta method with fixed time-step [15]. The numerical integration is performed under the initial conditions $\mathbf{x}(t=0) = [0,0,0]$ and $\mathbf{u}(t=0) = [0,0,0]$, and the boundary condition $z = z_{max}$ at $t = t_{final}$, where z_{max} is the depth of tank. As the time taken to reach z_{max} is unknown for any given release, the equations are integrated for a large enough time that the particle has dropped further than z_{max} and the time at which z_{max} is reached, along with the location vector $\mathbf{x} = [x, y, z_{max}]$, is calculated by interpolating the trajectory data on to $z = z_{max}$.

At the beginning of each simulation the initial values of the random variables C_D, C_L, α and θ are randomly generated from the distributions described above. Then, at the end of each time-step, the values are randomly perturbed before the next time-step in the integration. To avoid drastic changes in the magnitude of each of these parameters (e.g. α), the new values are generated randomly from a continuous uniform distribution over a pre-specified range ($\pm\delta\alpha$) about the previous value. So, the new values of C_D, C_L, θ and α are generated randomly from $\pm\delta C_D$, $\pm\delta C_L$, $\pm\delta\theta$ and $\pm\delta\alpha$ ranges about the previous values of the corresponding parameters. To illustrate the idea, consider the case where the value of C_D from the previous time step was 0.55 and δC_D has a fixed value of 0.03 for that simulation. Then, the new value of C_D for the next time step, will be randomly generated from a uniform distribution between $C_D - \delta C_D$ and $C_D + \delta C_D$, or 0.52 and 0.58 for this example. The same perturbation approach

is used for C_L, θ and α.

These random perturbations of C_D, C_L, α and θ at each time-step are to account for changes in orientation that alter the projected area ($\delta\alpha$), the magnitude of the drag and lift forces (δC_D and δC_L) and the direction of the lift force ($\delta\theta$). Over the course of a given set of flight simulations, the statistical distribution of the gravel landing locations will depend on the magnitude of the perturbations (δC_D, δC_L, $\delta\alpha$ and $\delta\theta$) and the number of times that the values are perturbed ($N = T/\delta t$) where T is the time taken to reach $z = z_{max}$ and δt is the integration time-step. To minimize the number of model parameters, the time-step was fixed for all simulations and was taken to be the time taken for the equivalent sphere to fall one radius when traveling at its terminal velocity U_T. The terminal velocity was calculated using the median value of the $C_D = 0.6$ to yield

$$U_T = \sqrt{\frac{2(F_w - F_B)}{C_D \rho A_e}} \tag{16}$$

and a time-step of

$$\delta t = \frac{R_e}{U_T}. \tag{17}$$

Therefore, the time scale is characteristic of a typical gravel piece within a given gradation and is consistently defined over all gradations.

The ranges of C_D, C_L, and α are determined from laboratory measurements of gravel geometry (section 2) and wind tunnel measurements of the force coefficients [14]. The equivalent sphere properties (m and R_e) are also calculated from measurement data. Therefore, the only unknown parameters in the model are δC_D, δC_L, $\delta\alpha$ and $\delta\theta$. These four parameters are used as fitting parameters to match the simulated landing locations with the experimental data.

5. Model results and comparison

The numerical studies were carried out for different combinations of the four fitting parameters discussed in previous chapter. The perturbation ranges δC_D,δC_L and $\delta\alpha$ were varied from 0 to 50% of the overall range of the respective

parameter in increments of 2.5% of the overall range while $\delta\theta$ was varied from 0 to 60^o in 1.5^o increments. This leads to a total of 21 values for each perturbation parameter except for $\delta\theta$ which has 41 values. To capture all possible combinations of these four parameters, a total of $21^3 \times 41$ simulations were run for each drop with 200 drops per case and for all five gradations. This resulted in a total of almost 380 million drop simulations.

The numerical results for each combination of parameters were compared to the experimental measurements described in section 3. For each gradation, the set of fitting parameters that yields the minimum error was extracted as an optimum set of model parameters. To show how the other combinations yield less desirable results compared to the optimized combination of the parameters the model was run with the perturbations turned off. Figure 11(a) shows a scatter plot of the resulting numerical and experimental landing locations for the largest gravel size (gradation A). Figure 11(b) shows a quantile plot of the radial distance showing the model radial distances plotted against experimental. The solid red line has a slope of 1 representing exact agreement between the experiments and the model. Both these plots are for when the model was run with the perturbations turned off so that the model spread is only due to the changes in randomly assigned initial conditions. It is clear from this set of plots that the spread obtained from this iteration of the model does not resemble the experimental data at all.

5.1. Optimization Technique

For all the combinations of fitting parameters, the numerical simulations give us the x and y coordinates of landing locations for 200 drops per gravel size. The radial distances of each landing location from the center of the tank were then calculated from the coordinates. From this, the mean and the standard deviation of the radial distances were calculated. To find an optimized combination of δC_D,δC_L, $\delta\theta$ and $\delta\alpha$, the absolute differences between the two means (numerical and experimental) and the two standard deviations are calculated. These two quantities are not to be minimized independently since they are not exclusive

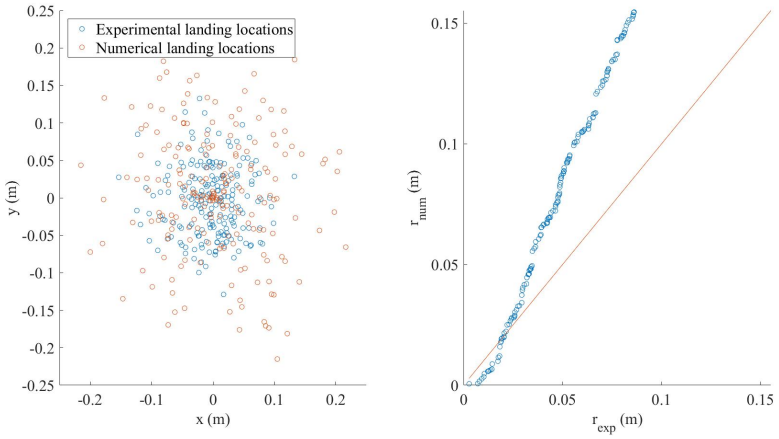

Figure 11: (a) Scatter plot of landing locations obtained from the model and experimental results for the case when the perturbations were set to zero (b) Quantile plot of the radial distance for the same data. Both plots are for gradation A.

of each other. For example, a very localized spread (meaning the standard deviation is smaller) can yield a mean which can be the same as another spread that is less localized (i.e. with higher standard deviation). To optimize both these quantities, an optimization parameter (ϵ) was introduced that quantified the difference between the means and standard deviations of the model and experimental data. Two versions of ϵ were investigated. The first was the sum of the squares of the differences in the means and standard deviations,

$$\epsilon_D = \sqrt{(r_{exp} - r_{model})^2 + (\sigma_{r.exp} - \sigma_{r.model})^2}. \tag{18}$$

The second was these differences normalized using the experimental values for the mean and standard deviation,

$$\epsilon_R = \sqrt{\left(1 - \frac{r_{model}}{r_{exp}}\right)^2 + \left(1 - \frac{\sigma_{r.model}}{\sigma_{r.exp}}\right)^2}. \tag{19}$$

To calculate the optimal set of perturbation values for a given gravel gradation, the values of both ϵ_D and ϵ_R were calculated for all 379,701 unique combinations of the perturbation values and the minimum found. For three out of the five gravel sizes the optimized set of perturbation parameters were the

same for each definition of ϵ. However, for gradations B and C, the optimized cases were different for the two definitions of ϵ. Figure 12 shows quantile plots for three realizations of the optimization method using each definition of ϵ. In each case 150 sample radial distances were randomly selected from the experimental and numerical data sets and the values of ϵ_D and ϵ_R were calculated. The optimal combination of perturbations was then calculated and a quantile plot was developed in which the remaining 50 experimental data points were plotted against the remaining 50 model points for the optimal set of perturbations.

To understand which of the two optimization techniques yields results closest to the experimental radial distances, t-tests were performed between the experimental and the numerical radial distances for the optimized cases for each definition. The t-tests results show that there exists no statistically significant difference (p-value $<$ 5% significance level) between the two means under the assumption of equal variances, regardless of the optimization approach. Next, the R-squared value was calculated as a measure of predictive accuracy for both pairs, i.e. experimental vs numerical optimized based on (18) and (19). The results showed that the optimization using the minimum value of (19) consistently outperformed the other approach (18). Based on this analysis, the approach in equation (19) is used in this study as the optimization technique.

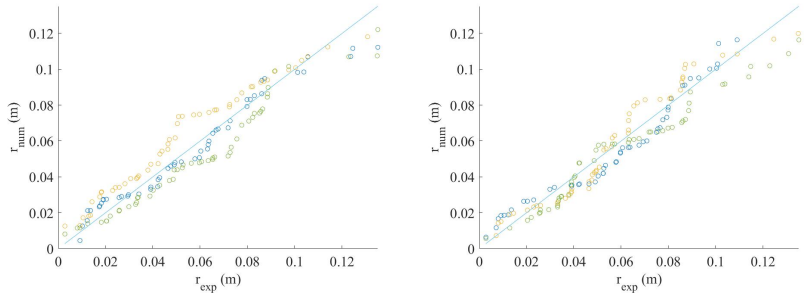

Figure 12: Quantile plots of radial distance for 50 drops with experimental results on the horizontal axis and numerical results on the vertical axis for the optimized perturbation values generated from a separate set of 150 drops. (Left) Model optimization based on ratios (19) and (right) model optimization based on differences (18)

.

The value of the optimization parameter as a function of each perturbation was plotted in Figure 13 to illustrate the significance of the role played by each perturbation. In each plot three of the perturbation parameters were held constant at their optimal values and then ϵ was plotted as a function of the remaining parameter. For all four plots there is variability along the lines due to the finite size of the data sets used in the optimization. However, despite this noise, there are clear minima for two of the parameters, namely $\delta\theta$ and δC_L. For $\delta\alpha$ and δC_D the minima are less distinct relative to the noise. This was reflected in the perturbation values in the multiple optimization runs used to develop Figure 12. Each time the optimization was run the optimal values of $[\delta C_D, \delta C_L, \delta\theta, \delta\alpha]$ changed. However, the changes in $\delta\theta$ and δC_L were small and centered around the values shown in Figure 13 whereas the values of $\delta\alpha$ and δC_D varied over a wider range.

	Gradations				
	A	B	C	D	E
δC_D	0.01	0.15	0.04	0.00	0.00
δC_L	0.0525	0.0175	0.04375	0.035	0.0175
$\delta\theta$ (degrees)	42.0	46.5	42.0	49.5	52.5
$\delta\alpha$ (% of $\alpha_{max} - \alpha_{min}$)	0.117 (10%)	0.231 (20%)	0.447 (37.5%)	0.267 (22.5%)	0.685 (42.5%)
Exp. Mean (mm)	58.3	44.8	50.3	44.2	31.1
Model Mean (mm)	58.3	44.9	50.3	44.2	31.1
Exp. σ (mm)	30.8	29.6	29.7	27.8	21.8
Model σ (mm)	30.8	29.6	29.7	27.8	21.8
ϵ_R	0.00088	0.0019	0.00073	0.0013	0.0018

Table 3: Optimized combinations of the perturbation parameters and the resulting means and standard deviations obtained from the model for all gradations.

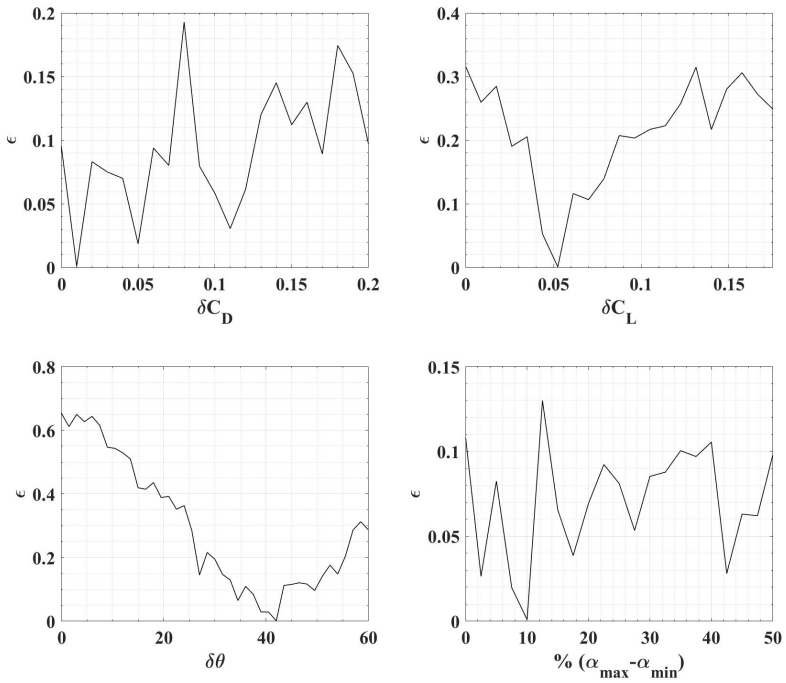

Figure 13: Plots of the optimization parameter ϵ as a function of each perturbation parameter. In each plot the three of the four perturbation parameters are held at their optimized values and the fourth one plotted. From top left reading across then down δC_D, δC_L, $\delta\theta$, and $\delta\alpha$ expressed as a percentage of $\alpha_{max} - \alpha_{min}$. All plots are for Gradation A

Having established that using ϵ_R (19) provided a marginally better result than ϵ_D (18), this technique was used to establish the optimal values of $[\delta C_D, \delta C_L, \delta\theta, \delta\alpha]$ using all 200 experimental data points per gradation. The results of these optimizations are shown in Table 3. From these data, we can see that for the optimized condition, δC_L has, albeit small, finite non-zero values. The perturbation of θ (which models the lift force direction), however, has large magnitudes for each gradation under the optimized condition. These indicate that, to replicate the experimental spread of landing locations numerically, the lift force has to be modeled in such a way that at the end of every time step during the flight of a gravel piece, the magnitude of lift coefficient and the direction of the lift

force has to be perturbed. However, the optimization suggests that there is only a small variation in the magnitude of the lift force (small δC_L) and that the main impact of changes in gravel orientation during flight is to change the direction of the lift force (large $\delta\theta$). Thus, the numerical model presented in this study quantitatively shows that the lift force vector has a significant role on the flight of irregularly shaped gravels, while the standard debris flight equations fail take such effects into account due to the inherent assumption of sphericity [9, 10].The variation in δC_D and α seen in Figure 13 make it difficult to draw conclusions about their role in the gravel flight.

Figure 14 illustrates the agreement between the model and experimental data for the optimized case calculated using all 200 data points for gradation C. Figure 14(a) shows a scatter plot of landing locations obtained from the optimized combination of $[\delta C_D, \delta C_L, \delta\theta, \delta\alpha]$ along with the experimental data. Figure 14(b) shows a quantile plot of the radial distances (experimental vs numerical) of landing locations for the same case. The solid red line is the line of exact agreement between the experimental and numerical data points.

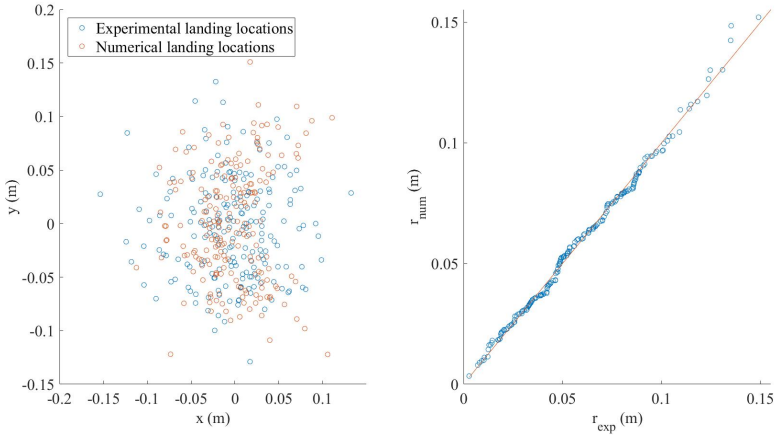

Figure 14: (a) Spread of landing locations obtained from the model in comparison with experimental spread, (b) Comparison of radial distances obtained from model with respect to experimental radial distances. Both plots are based on the optimized combination of perturbation parameters for Gradation C.

In Figure 15, the comparison of experimental and numerical radial distances obtained from the optimized combination of perturbation parameters for each gravel gradation are shown. The figure shows that, for the optimized model, the numerical data are in good agreement with the experiments.

6. Conclusions

A simple set of experiments in which gravel pieces are dropped in a tank full of stationary water demonstrated that the standard compact debris flight models are inappropriate for gravel flight. The experiments showed that gravel does not fall vertically but rather has a more complex trajectory in which the gravel orientation changes during flight and there are both lift and drag forces acting on the debris. Standard compact debris flight models ignore lift forces and assume a constant cross sectional area [10, 9]. To overcome these limitations, a stochastic model was developed in which the lift and drag coefficients, projected area, and orientation of the lift force are all varied randomly during flight. The frequency at which these parameters were perturbed was set based on the size and terminal velocity of the gravel gradation. The model was run for a range of perturbation magnitudes and an optimal set of perturbation parameters was established (Table 3). The results of the optimized model show very good agreement with the measurements from the experimental drops (Figure 15).

The model developed was validated against a set of experiments in which gravel pieces were dropped through stationary water. It is worth discussing the limitations of this approach. In water, the buoyancy force relative to the gravel weight will be much larger compared to gravel in air. This, along with the higher fluid density increasing the drag and lift forces, resulted in much lower terminal velocities (of the order of U_{term} $0.5m/s$) compared to gravel falling through air (U_{term} $10-15m/s$). Therefore, the Reynolds number in the water experiments will be about a factor of 2-3 less than the same particle falling in air ($O(3,000)$ in water compared to $O(10,000)$ in air). Both these Reynolds numbers would be within the Reynolds number independent range for a sphere [16] so the force

coefficients are likely independent of the Reynolds number and will be similar in air and water. The other limitation is that the tests were run in a stationary ambient whereas windborne debris flight occurs in an ambient wind field. The inclusion of a wind field in the model is simple as the model is built modeling the location and velocity vectors. However, it is possible that the values of the optimal perturbations may be different from those in Table 3 and testing in air with an ambient wind field should be completed.

The inclusion of an ambient wind field will add an additional source of trajectory variation due to turbulent gusts in the wind field. Karimpour & Kaye (2012) [17] simulated spherical particles in a turbulent flow and showed that the mean trajectory increases with increasing turbulent intensity but decreases if the vertical and horizontal fluctuations are negatively correlated. It is unclear if the trajectory variation due to gravel orientation (the subject of this study) or due to turbulent fluctuations in the wind field will have a bigger impact on the overall variability in the landing location. This topic is left to future study.

The model presented will improve the prediction of flight distance for windborne gravel. The inclusion of a lift force will lead to flight distances that are greater than those predicted using the standard two dimensional models. This would be important in predicting the risk of gravel impact on a building facade due to gravel blow-off from an upwind structure.

Acknowledgements

The authors gratefully acknowledge the insights provided by Dr. Abdul A. Khan. The authors would also like to thank Megan Holmes for her work on the experiments and data collection. This material is based upon work supported by the National Science Foundation under Grant No. 1760999. Any opinions, findings, and conclusions or recommendations expressed in the material are those of the author and do not necessarily reflect the views of the NSF.

References

[1] J. E. Minor, Lessons learned from failures of the building envelope in windstorms, J. Architectural Eng. 11 (1) (2005) 10–13.

[2] T. L. Smith, J. R. McDonald, Roof wind damage mitigation: Lessons from hugo, in: B. L. Sill, K. P. Sparks (Eds.), Hurricane Hugo 1 Year Later, Proceedings of a Symposimn and Public Forum held in Charleston, September 13-15, 1990, South Carolina, American Society of Civil Engineers, New York, 1991, pp. 224–229.

[3] P. R. Sparks, S. D. Schiff, T. A. Reinhold, Wind damage to envelopes of houses and consequent insurance losses, J. Wind Eng. & Ind. Aero. 53 (1994) pp. 145–155.

[4] R. A. Behr, J. E. Minor, A survey of glazing system behavior in multi-story buildings during hurricane andrew, The Structural Design of Tall Buildings 3 (3) (1994) 143–161. doi:10.1002/tal.4320030302.

[5] National Hurricane Center, Hurricanes in history, Tech. rep., N.O.A.A.
URL https://www.nhc.noaa.gov/outreach/history/

[6] A. Kareem, R. Bashor, Performance of glass/cladding of high-rise buildings in hurricane katrina, The Wind Engineer (Newsletter of AAWE) (2006) 1–5.

[7] K. Bergen, Strategic hotel capital estimates hyatt regency new orleans losses due to storm damage and lost business could exceed $100 million, Chicago Tribune October 1st (2005).

[8] J. Wills, B. Lee, T. Wyatt, A model of wind-borne debris damage, J. Wind Eng. & Ind. Aero. 90 (2002) 555–565.

[9] C. J. Baker, The debris flight equations, J. Wind Eng. & Ind. Aero. 95 (2007) 329–353.

[10] J. Holmes, Trajectories of spheres in strong winds with application to windborne debris, J. Wind Eng. & Ind. Aero. 92 (2004) 9–22.

[11] AMsterCHEN, https://www.amsterchem.com/scanit.html.

[12] A. Tohidi, N. B. Kaye, Aerodynamic characterization of rod-like debris with application to firebrand transport, J. Wind Eng. & Ind. Aero. 168 (2017) 297–311.

[13] M. Grayson, W. Pang, S. Schiff, Three-dimensional probabilistic windborne debris trajectory model for building envelope impact risk assessment, Journal of Wind Engineering and Industrial Aerodynamics 102 (2012) 22–35.

[14] V. Chai, D. Parkhi, S. Boopathy, J. Xiang, J. Schluter, A model for the aerodynamic coefficients of rock-like debris, Comptes Rendus Mécanique (nov 2018). doi:10.1016/j.crme.2018.10.001.

[15] V. S. Amos Gilat, Numerical Methods for Engineers and Scientists, John Wiley & Sons Inc, 2013.
URL https://www.ebook.de/de/product/20592408/amos_gilat_vish_subramaniam_numerical_methods_for_engineers_and_scientists.html

[16] P. K. Kundu, I. M. Cohen, H. H. Hu, Fluid mechanics, Academic Press, 2002.

[17] A. Karimpour, N. Kaye, On the stochastic nature of compact debris flight, J. Wind Eng. & Ind. Aero. 100 (1) (2012) 77–90.

Appendix A. MANOVA of gravel shape

In order to assess our qualitative observation that the distributions of L_1/L_3 and L_2/L_3 differed across gradations, discussed in section 2, multivariate analysis of variance (MANOVA) has been performed (using IBM SPSS Statistics

27.0). MANOVA is a method of performing a formal hypothesis test of mean differences across gradations using two (or more) dependent variables simultaneously. The two dependent variables in this case were L_1/L_3 and L_2/L_3. This is an extension of univariate analysis of variance (ANOVA) which is a method of performing a formal hypothesis test of mean differences across gradations for one dependent variable.

The underlying assumptions for MANOVA are:

- Absence of multivariate outliers
- Linearity
- Equality of covariance matrices

Absence of multivariate outliers is checked by assessing the Mahalanobis Distances among the MANOVA model residuals. In our analysis, the maximum Mahalanobis Distance was 9.444, which was less than the critical value based on a chi-square distribution. Therefore, we did not have any multivariate outliers. The assumption of a linear relationship between the dependent variables was assessed with a scatterplot matrix using JMP® Pro 14 between the two dependent variables (Figure A.16). The scatterplots suggested the relationship between L_1/L_3 and L_2/L_3 was linear for all gradations. The assumption of equality of covariance matrices across gradations is checked by Box's M test. For this test, we obtained a p-value of 0.259 suggesting the covariance matrices were similar across the gradations.

Table A.4 summarizes the MANOVA results. All test statistics resulted in p-values less than 0.05 suggesting differences in the L_1/L_3 and L_2/L_3 means across the gradations. To determine which of the two dependent variables contribute to this difference, single-factor ANOVAs were performed separately on L_1/L_3 and L_2/L_3. The results are shown in Table A.5. The univariate ANOVAs both produced p-values less than 0.05. This suggests that L_1/L_3 means differ across gradations and L_2/L_3 means differ across gradations, thus indicating that both L_1/L_3 and L_2/L_3 contribute to the significant differences across the gradations.

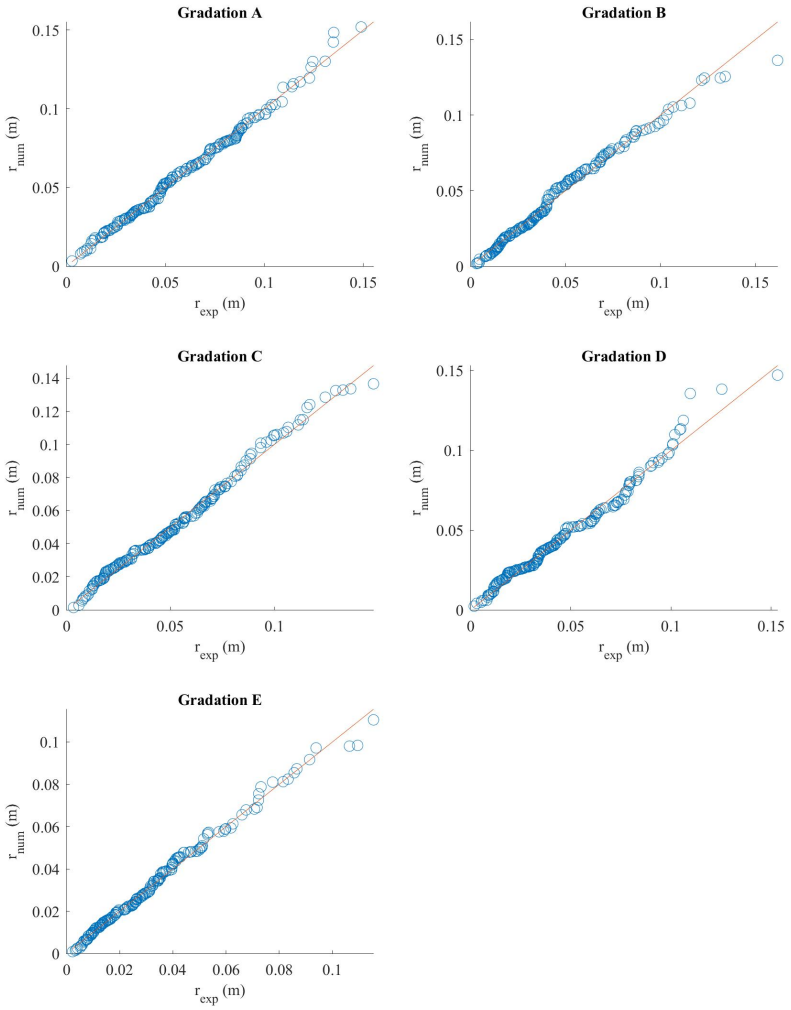

Figure 15: Comparison between numerical and experimental radial distances for all gradations using the optimal perturbation results shown in Table 3

.

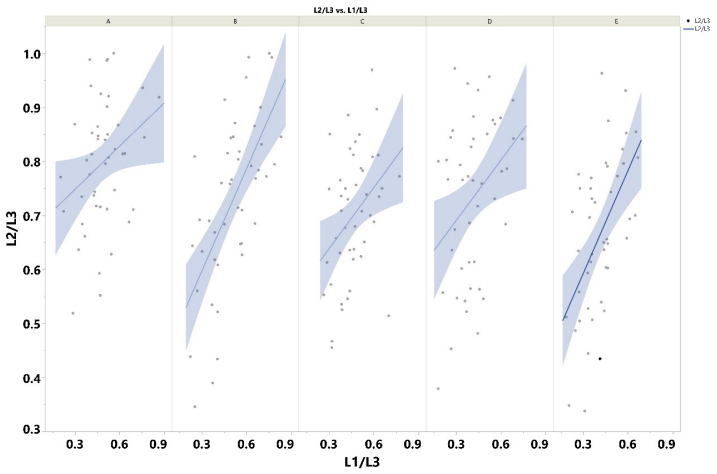

Figure A.16: Scatter plot matrix to check linearity between the two dependent variables. (Gradations A-E from left to right).

Effect	Value	F	Hyp. df	Err. df	Sig.	η_p^2	Noncent.	Observ. Power
Grades								
Pillai's Trace	.158	4.70	8.00	440	.000	.079	37.6	.998
Wilks' Lambda	.848	4.69	8.00	438	.000	.079	37.5	.998
Hotelling's Trace	.171	4.67	8.00	436	.000	.079	37.38	.998
Roy's Largest Root	.101	5.53	4.00	220.0	.000	.091	22.1	.976

Table A.4: Summary of single-factor multivariate analysis of variance (MANOVA)

Source	Dependent Variable	Type III Sum of Squares	df	Mean Square	F	Sig.	η_p^2	Noncent. Parameter	Observed Power
Grades	L_1/L_3	.31	4	.08	4.12	.003	.07	16.46	.91
	L_2/L_3	.43	4	.11	5.51	.000	.09	22.06	.98

Table A.5: Summary of univariate tests